Journal of Materials Research and Technology 40 (2026) 2278–2290

Contents lists available at ScienceDirect

Journal of Materials Research and Technology

journal homepage: www.elsevier.com/locate/jmrt

Biological activity of mullite macrospheres for bone tissue regeneration

Crislayne G. Andreto [a,*], Luísa Fialho [b], Magna Monteiro [c], Tiago P. Ribeiro [b], Leandro Fernandes [a], Joana Barros [b], Fernando J. Monteiro [b], Sandra Carvalho [d], Rafael Salomão [a]

[a] Materials Engineering Department – São Carlos School of Engineering, University of São Paulo, Avenida Trabalhador São-carlense 400, CEP, 13566-590, São Carlos, SP, Brazil
[b] i3S-Instituto de Investigação e Inovação em Saúde, Universidade do Porto, Portugal
[c] Laboratorio de Materiales Cerámicos, Grupo de Investigación en Bio y Materiales, Facultad Politécnica, Universidad Nacional de Asunción, Central, San Lorenzo, Paraguay
[d] CEMMPRE, ARISE, Department of Mechanical Engineering, University of Coimbra, 3030-788, Coimbra, Portugal

ARTICLE INFO

Handling Editor: P.Y. Chen

Keywords:
Bioceramic macrospheres
Gelcasting
Ionotropic gelation
Mullite

ABSTRACT

The development of ceramic bone graft substitutes that combine mechanical strength, biocompatibility, and interconnected porosity remains a challenge, particularly for injectable applications. Mullite ($Al_6Si_2O_{13}$) is a ceramic of particular interest due to its biocompatibility, chemical stability, and moderate mechanical properties; however, its use as a loose-fill implant has not yet been well explored. In this study, Al_2O_3–SiO_2 macrospheres were fabricated via ionotropic gelcasting, using sodium alginate as the binder and colloidal silica as the silica source. Three compositions were investigated: Al_2O_3-rich, stoichiometric mullite, and SiO_2-rich. Thermal treatments at 1500 °C yielded mullite, cristobalite, and residual alumina in different ratios. All samples exhibited high sphericity and inter-sphere macroporosity, favorable for loose-fill bone graft applications. The stoichiometric mullite macrospheres demonstrated the most balanced combination of specific surface area, microhardness, abrasion resistance, and compressive strength. In vitro assays confirmed the absence of cytotoxic and hemolytic effects and demonstrated support for osteoblast adhesion, proliferation, and alkaline phosphatase activity. These findings indicate that Al_2O_3–SiO_2 macrospheres, particularly stoichiometric mullite, are promising candidates for granular bone graft substitutes, offering a combination of structural integrity and biological performance suitable for bone tissue regeneration.

1. Introduction

A wide range of bioceramic materials is currently being developed for use in tissue regeneration and drug delivery, with characteristics tailored to their specific applications, particularly in the form of loose-fill implants [1]. Calcium phosphates ($Ca_3(PO_4)_2$) are among the most extensively studied bioactive ceramics [1–5], while alumina (Al_2O_3) and zirconia (ZrO_2) are widely studied as bioinert materials [5–11]. The functionality and the inclusion of other materials or trace elements are essential points to enhance these materials' properties, as well as the development of new bioceramics or the optimization of synthesis processes. Biomaterials, such as calcium silicate ($CaSiO_3$ or β-Wollastonite), which have bioactivity and degradability properties, are suitable for bone tissue regeneration [12,13]. Zhang et al. (2013) reported that the functionalization of the $CaSiO_3$ with iron (Fe) resulted in a multifunctional mesoporosity magnetic biomaterial suitable for bone regeneration, local drug delivery, and magnetic hyperthermia [13]. Ismail et al. (2021) studied how mullite ($3Al_2O_3{\cdot}2SiO_2$), maghemite (γ-Fe_2O_3), and silver (Ag) nanoparticles would improve the tensile strength, magnetism, bioactivity, and antimicrobial activity of β-Wollastonite. They reported that each dopant material improved one property, particularly at 20 wt% Mullite, which boosted compressive strength by up to 200 % making it suitable for cancellous bone applications [14].

Macrospheres are low-aspect-ratio, spherically-shaped materials with diameters ranging from 1 to 10 mm. Due to their loose-fill shape, they can access complex geometric areas, working as scaffolds with the spheres serving as the solid part and the vacancies between them as the porous phase. Several routes can produce spheres, including chemical reactions [15], sol-gel [16,17], spray-drying [18,19], foaming [20], and

* Corresponding author.
E-mail addresses: crislayne.andreto@usp.br (C.G. Andreto), rsalomao@sc.usp.br (R. Salomão).

https://doi.org/10.1016/j.jmrt.2025.12.307
Received 25 November 2025; Received in revised form 26 December 2025; Accepted 30 December 2025
Available online 31 December 2025

Table 1
Physicochemical characteristics of the raw materials used for the fabrication of Al_2O_3–SiO_2 macrospheres, including chemical purity, particle size distribution, density, and specific surface area.

Characteristics	**Calcined Alumina (CA)**[a]	**Colloidal Silica (CS)**[b]
Composition (wt.%)	α-Al_2O_3: 99.80; Na_2O: 0.07; Fe_2O_3: 0.02; MgO: 0.05; SiO_2: 0.03; CaO: 0.02.	SiO_2: 99.90; Na_2O: 0.01.
Main crystalline phase (PDF file)	α-Al_2O_3 (46–1212)	SiO_2 (non-crystalline)
Particle Size (D_{10}, D_{50}, D_{90})	0.27, 1.13, 14.02 [μm]	11.31, 54.10, 87.08 [nm]
Solid Density [ρ, g. cm^{-3}]	4.05	2.20
Specific surface area [$m^2.g^{-1}$]	8.20	80.00
Solid content [wt%]	–	50
Viscosity [cP]	–	8.00

[a] After thermal treatment at 1000 °C.
[b] After drying at 120 °C.

ionotropic gelation [21–23]. Ionotropic gelation stands out for its versatility and low cost, enabling the production of dense or porous structures from powders with varying particle sizes, resulting in pure or composite final products with good homogeneity and minimal defects. The spheroidization technique has been widely standardized to produce improved organic and inorganic sphere materials [23–25]. This technique consists of the consolidation and immobilization of particles through the formation of a polymeric network, produced by *in-situ* polymerization of organic monomers previously dissolved in stable suspensions in the presence of cross-linking agents [22,26].

Alumina (Al_2O_3) is a well-known bioceramic due to its good stability in physiological environments, biocompatibility, and high resistance to compression and wear [6,8,27–29]. However, due to its low bioactivity, numerous studies attempted to combine Al_2O_3 with bioactive materials, such as hydroxyapatite [30–33], bioglass [34,35], keratin [36,37], silk fibroin [38], and chitosan [7,11]. Similarly, studies involving SiO_2 composites are common in nanomedicine, particularly when combined with other biomaterials to improve bioactivity [4,39,40] or develop efficient drug delivery systems [15,19]. Additionally, mullite, a stable phase within the Al_2O_3–SiO_2 system, is of particular interest due to its biocompatibility, chemical stability, and moderate mechanical properties. The biocompatibility of its constituent phases supports its potential as a biomaterial [41,42]. Over the past decades, mullite has been studied as a mechanical reinforcement [2,43] and, more recently, as an antimicrobial agent [44]. Although it has not yet been explored as a bone graft substitute, its cytocompatibility suggests promising potential for this application [42,45].

To meet the demands of bone graft substitutes, such as porosity for cell growth, vascularization, along with mechanical integrity and bioactivity, tailored microstructures and compositions are essential. The production of spherical ceramic granules with interconnected macroporosity can enhance implant packing, nutrient diffusion, and cell migration, thereby enhancing their suitability for bone defect repair. Nevertheless, achieving controlled porosity and phase composition while maintaining adequate mechanical and biological properties remains a significant challenge. This study aimed to produce Al_2O_3–SiO_2 macrospheres using calcined alumina and colloidal silica. The macrospheres were produced by ionotropic gelcasting through an aqueous co-dispersion of calcined alumina and colloidal silica, employing sodium alginate as a binder. After drying and thermal treatments, macrospheres were characterized regarding their meso- and macroporosity distribution. Thermogravimetric and dilatometric analysis were conducted, along with microstructural, morphological, and mechanical strength characterizations. *In vitro* cytotoxicity, hemocompatibility, metabolic activity, cell adhesion, and alkaline phosphatase activity assays were performed to evaluate the biological response. The results provide insights into the design of ceramic spheres for potential use as injectable or loose-fill bone graft materials.

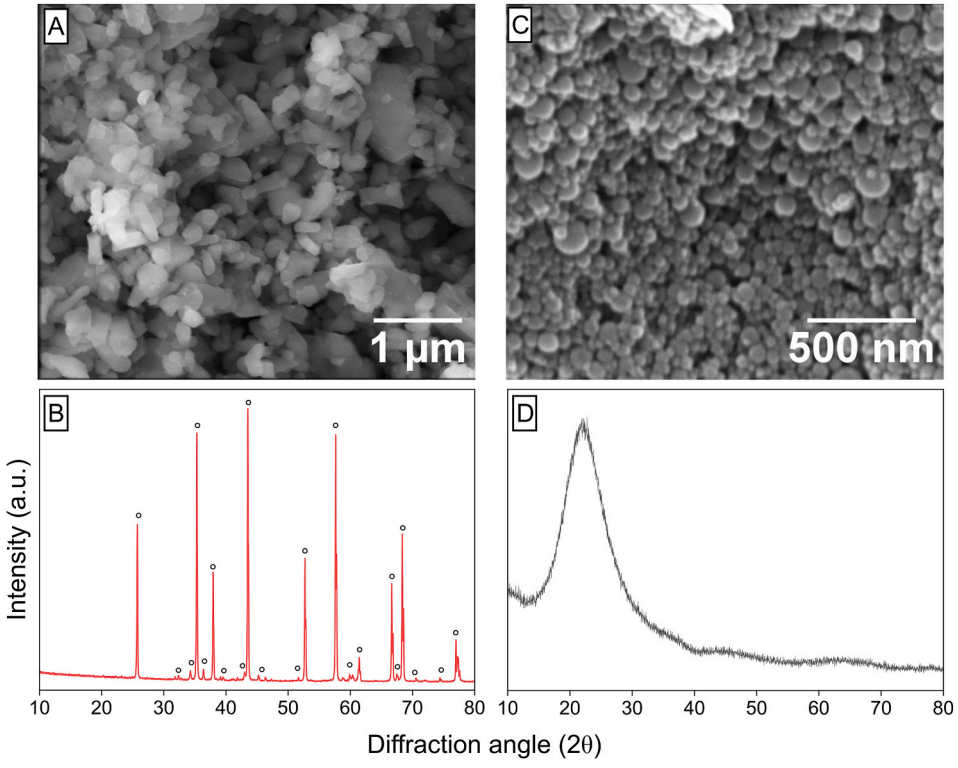

Fig. 1. SEM micrographs and XRD patterns of the raw materials used for macrosphere fabrication. (A, B) Calcined alumina (A1000SG: Corundum, JPCDS 1–1243). (C, D) Colloidal silica (Levasil CS 5028).

Table 2
Chemical composition design of the Al_2O_3/SiO_2 ceramics investigated, expressed in mol% and wt% to illustrate variations from stoichiometric mullite toward alumina- or silica-excess formulations.

Samples identification	Composition tested	Al_2O_3 [mol/wt %]	SiO_2 [mol/wt %]
3A1S (excess of alumina)	75 % mol Al_2O_3 25 % mol SiO_2	3/83.58	1/16.42
3A2S (stoichiometric mullite)	60 % mol Al_2O_3 40 % mol SiO_2	3/71.79	2/28.21
3A3S (excess of silica)	50 % mol Al_2O_3 50 % mol SiO_2	3/62.92	3/37.08

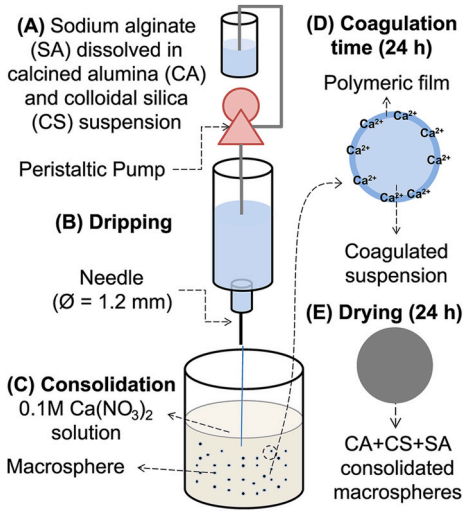

Fig. 2. Ionotropic gelation process for the production of alumina-silica macrospheres. (A) is the preparation of ceramic/polymer suspension; (B) dripping process into a 1.2 mm needle ;(C) consolidation in a 0.1 M $Ca(NO_3)_2$ solution; (D) spheres remain 24 h in the gelling solution for formation of a polymeric film; (E) after washing, spheres are dried (60 °C, 24 h), obtaining the consolidated macrospheres.

2. Materials and methods

2.1. Preparation of suspensions

Al_2O_3/SiO_2 suspensions (Table 1) were prepared using distilled water, calcined alumina (CA, α-Al_2O_3, A1000SG, Almatis, USA), colloidal silica dispersions (CS, synthetic amorphous SiO_2, Levasil CS5028, Nouryon South América, Brazil), and sodium alginate (SA, $C_6H_7O_6$, Synth, Brazil) as a binder. A dispersant (poly(carboxylate ether), FS 20 Castment, BASF, Germany) and an anti-foam agent (Tensiol, Lamberti, Brazil) were added to improve particle individualization and prevent trapped air bubbles, respectively. A bath of calcium nitrate ($Ca(NO_3)_2.4H_2O$, Êxodo Científica, 0.1 M) behaved as a coagulating agent.

All raw materials were previously characterized regarding composition (X-ray dispersive spectroscopy, Shimadzu, EDX 720), morphology (SEM, FEG-SEM Inspect-F50, FEI Company, the samples were fixed in carbon tape and sputter-coated with platinum (Q150R sputter, Quorum Technologies) for 1 min, Fig. 1A and B), crystalline phases (X-ray diffraction, Rotaflex RV 200B, Rigaku- Denki Corp., with Cu Kα radiation (λ = 0.14506 nm), diffraction angle (2θ) scanned between 10° and 100°, rate of 2°min^{-1}) (Fig. 1C and D), particle size distribution ($D_{10}/D_{50}/D_{90}$, DT-1202, Dispersion Technology Inc.), solid density (99.999 % purity helium pycnometry - Ultrapyc 1200e, Quantachrome Instruments), and specific surface area (SSA, BET method, Nova 1200e, Quantachrome Instruments, ASTM C 1069-09 standard "Standard Test Method for Specific Surface Area of Alumina or Quartz by Nitrogen Adsorption" [46]).

The compositions tested (Table 2) were defined from different Al_2O_3–SiO_2 ratios based on their phase diagram [47]: a stoichiometric mullite composition ($3Al_2O_3{\cdot}2SiO_2$ or $Al_6Si_2O_{13}$), one condition with excess of Al_2O_3 ($3Al_2O_3{\cdot}1SiO_2$), and another with excess of SiO_2 ($3Al_2O_3{\cdot}3SiO_2$).

2.2. Synthesis of mullite macrospheres

The macrospheres were produced by dripping. Initially, sodium alginate (SA, 3 wt% of the total solids in suspension) was dissolved in distilled water (10 times the mass of SA). A 20 vol% of solids alumina suspension was prepared by adding calcined alumina (CA) powder and dispersant (0.1 wt%) in water. The mixture was ground in a ball mill (1:10 mass of solids/ZrO_2 spheres, 6 mm, 80 rpm; SL34/4, SOLAB, Brazil) for 2 h to break agglomerates. The alumina suspension was added to the polymeric solution and homogenized for 10 min with a paddle mixer (RW 20 digital, IKA, Germany). After this, colloidal silica was added to the suspension under stirring and homogenized for 10 min (Fig. 2A). Following, using a peristaltic pump (Masterflex ® L/S Easy-Load® II 77201-60, USA, Fig. 2B), the suspension was dripped in a 0.1 M $Ca(NO_3)_2$ coagulating bath (Fig. 2C), remaining during 24 h to complete coagulation (Fig. 2D) [22,29]. After this period, the samples were washed with water and ethyl alcohol 70 % and dried at 60 °C for 24 h (Venticell, MMM Group, Germany) (Fig. 2D). Macrospheres were thermally treated at a 5 °C.min^{-1} heating rate up to 1500 °C for 3 h (Lindberg Blue M, Thermo Fisher Scientific, USA).

2.3. Physicochemical characterization

The total porosity was evaluated by mercury intrusion porosimeter (PoreSizer 9320, Micrometrics) and Archimedes' Principle according to ASTM B962-23 "Test Methods for Density of Compacted or Sintered Powder Metallurgy (PM) Products Using Archimedes Principle" [48]. The dry mass (Md) was determined by weighing samples after drying for 24 h at 60 °C, for apparent mass (Map), the samples were submerged in water at room temperature for 24 h to fill the pores and then weighed submerged on distilled water; the humid mass (Mh) was determined removing excess liquid from the sample's surface and then weighing once more. The water density was obtained from the table of density as a function of temperature.

Density (ρ), relative density (ρ_r), and total porosity (P) were calculated by Eqs. (1)–(3), respectively:

$$\rho = M_d \;/\; \left(\left(M_h - M_{ap}\right) \times \rho_{H2O}\right) \tag{1}$$

$$\rho_r = 100 \times \left(\rho \;/\; \rho_{sol}\right) \tag{2}$$

$$P = 100 - \rho_r \tag{3}$$

The solid density (ρ_{sol}) was measured using a helium pycnometer (Ultrapyc 1200e, Quantachrome Instruments, USA) with ground powder samples.

The bulk density was determined by the ratio of mass and volume of spheres in a graduated cylinder (Uniglas 185.010, 10 ± 0.2 mL, Brazil); the apparent geometric density (AGD) was attained by the ratio of mass and volume of each sphere according to Eq. (4), and inter-sphere porosity by Eq. (5):

$$AGD = m \;/\; \left(4 \;/\; 3 \times \pi \times r_1 \times r_2 \times r_3\right) \tag{4}$$

$$\text{Inter} - \text{sphere porosity} = 100 \times \left(1 - \left(\text{bulk density} \;/\; AGD\right)\right) \tag{5}$$

Where r_1, r_2, and r_3 are the sphere radii on three different axes. The AGD was obtained by averaging ten measurements.

For the specific surface area (SSA, $m^2.g^{-1}$), and total pore volume

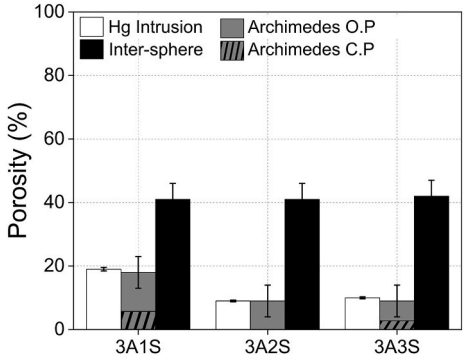

Fig. 3. – Total and inter-sphere porosity of alumina-silica macrosphere. White bars correspond to the intra-sphere porosity obtained by mercury intrusion porosimetry, grey bars represent the open intra-sphere porosity (O.P.) determined by Archimedes' Principle, dashed grey bars represent the close intra-sphere porosity (C.P) determined by Archimedes' Principle, and black bars indicate the inter-sphere porosity. Data are presented as mean ± standard deviation.

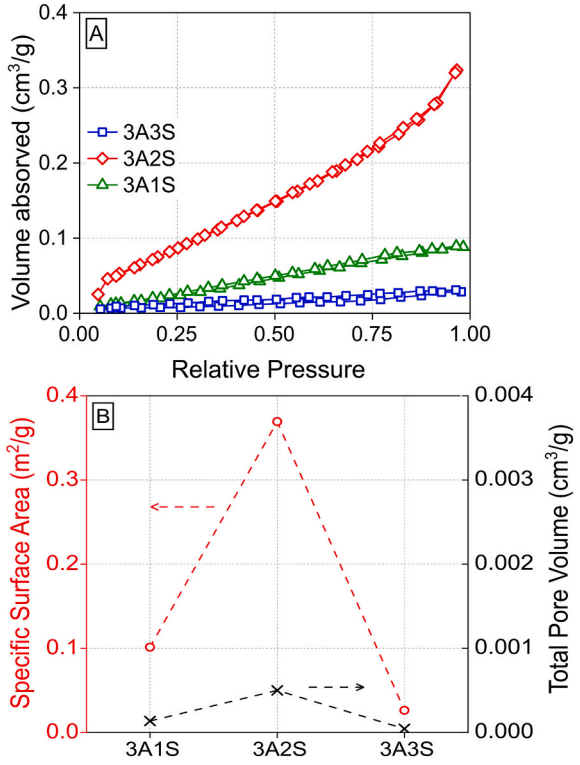

Fig. 4. – Nitrogen adsorption–desorption characterization of the alumina-silica macrosphere (A) Adsorption-desorption isotherms (BET method, 3A3S: blue □, 3A2S: red ◊, 3A1S: green Δ). (B) Specific surface area (BET method, red ○, left axis) and total pore volume (calculated at $P/P_0 \approx 0.99$, black × , right axis).

(TPV, $cm^3.g^{-1}$), the spheres were degassed for 2 h at 200 °C and measured by high-purity N_2 adsorption-desorption (BET method, NOVA 1200e, Quantachrome Instruments, USA) according to ASTM C 1069–09 "Standard Test Method for Specific Surface Area of Alumina or Quartz by Nitrogen Adsorption" [46].

Thermogravimetry analysis (TGA, Pyris 1, PerkinElmer, USA) was achieved on sodium alginate spheres at 600 °C, 5 °C.min^{-1} heating rate under an air atmosphere flowing at 20 mL min^{-1}, to evaluate polymer degradation. Differential scanning calorimetry (DSC, 404 F1, Netzsch, Germany) of the dry alumina/colloidal silica/SA macrospheres on the stoichiometric mullite composition (3A2S) was performed from room

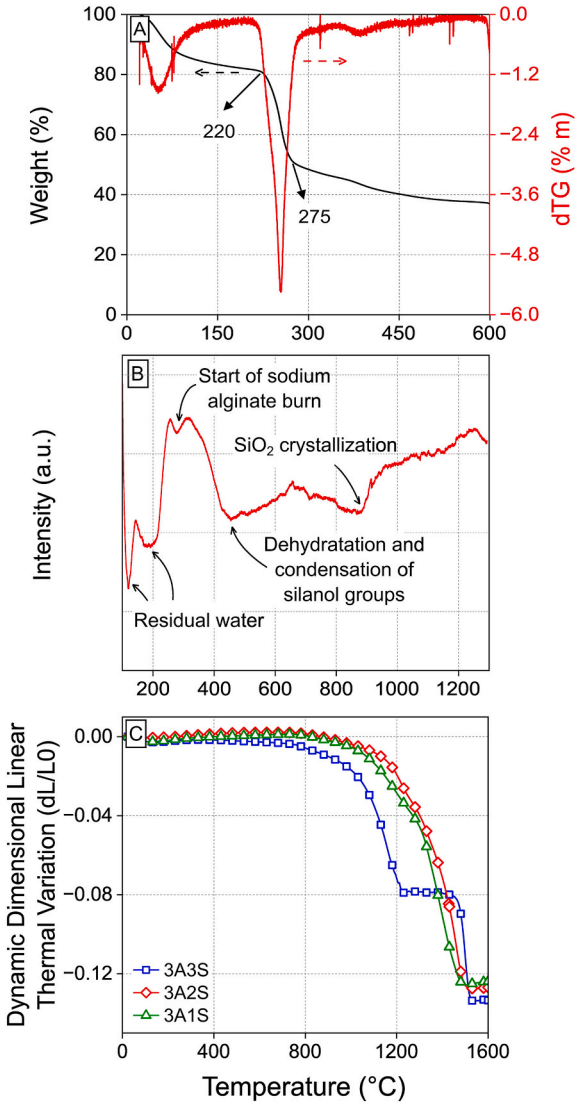

Fig. 5. – (A) Thermogravimetric analysis of sodium alginate sphere showing the mass loss profile during heating. (B) DSC of mullite macrosphere (3A2S) highlighting the thermal transitions of the composite system. (C) Dynamic linear shrinkage curves for the different compositions. Symbols: 3A3S: blue □, 3A2S: red ◊, 3A1S: green Δ.

temperature up to 1350 °C at a rate of 10 °C.min^{-1}. Dilatometric analysis (DIL402C, Netzsch, Germany) was conducted on green samples at 1600 °C for 3 h at a rate of 5 °C.min^{-1}. Spheres were ground and uniaxially pressed to produce cylindrical samples measuring 6 mm in diameter and 8 mm in length.

Identification of crystalline phases was carried out by X-ray Diffraction (XRD, Rotaflex RV 200B, Rigaku- Denki Corp.), with Cu Kα radiation ($\lambda = 0.14506$ nm), diffraction angle (2θ) scanned between 10° and 80°, rate of 5°min^{-1}, step of 0.02°s^{-1}, current intensity 30 mA and voltage 40 kV, using powder samples obtained by grinding. For Fourier-transformed infrared spectroscopy (FTIR, PerkinElmer Frontier spectrometer, USA), spheres were ground and analyzed by the KBr pellet technique in the spectral range region from 400 to 4000 cm^{-1}, with a 4 cm^{-1} resolution and 36 scans per sample.

2.4. Morphological properties

The morphology of the sintered samples was analyzed by scanning electron microscopy (SEM, Hitachi SU3800, Japan) at an accelerating

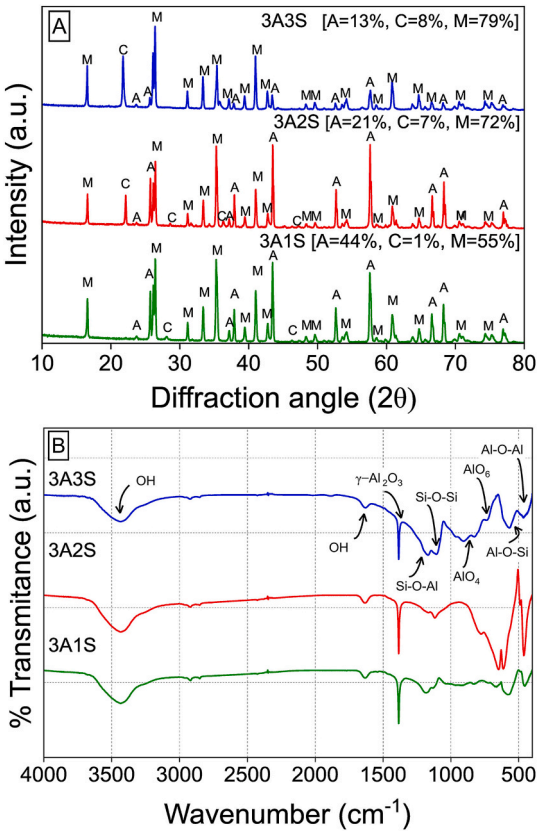

Fig. 6. (A) XRD diffractograms. Symbols: A: Al_2O_3 (Corundum, JPCDS 1–1243), C: SiO_2 (Cristobalite, JCPDS 1438), M: $Al_6Si_2O_3$ (Mullite, JCPDS 1–163), 3A3S: blue line, 3A2S: red line, 3A1S: green line. (B) FTIR spectra of the alumina-silica macrospheres sintered at 1500 °C.

voltage of 15 kV. The samples were fixed in carbon tape with a thin layer of graphite conductive adhesive and sputter-coated (Cressington Sputter Coater, 108 Auto, USA) with an Au/Pd alloy conductive film for 1 min. ImageJ software was used to evaluate the range of diameter, circularity, and roundness [21].

2.5. Mechanical characterization

Vickers microhardness was measured on polished cross-section by the indentation technique (Microhardness Tester VMHT MOT, Leica, Germany), according to ASTM C 1327-99 "Standard Test Method for Vickers Indentation Hardness of Advanced Ceramics" [49] with a diamond pyramid indenter applying 100 g for 15 s. For this, macrospheres were embedded in an unsaturated polyester resin, sanded and polished with successively finer grades of SiC sandpaper (#120, #320, #400, #600, #1200). The hardness results were the average of 10 measurements in different spheres.

The compression strength was measured in a universal testing machine (Model WDW-30E, 5 kN load cell, 0.5 mm min^{-1} crosshead speed, adapted from ISO 13503 [50]. For this, 1 g of spheres was compressed into a cylindrical matrix ($d_m = 15$ mm) at 30, 60, 80, 100, and 120 MPa. Each measurement was replicated 3 times. The compressive stress was calculated using Eq. (6). After each compression, the samples were sifted, the uncrushed samples were weighed, and the mechanical behavior was determined from the mass loss according to Eq. (7).

$$F = \pi \times \sigma \times d_m^2 \,/\, 4 \tag{6}$$

$$\text{Mass loss in compression} = (m_i - m_f) \;/\; m_i \times 100 \tag{7}$$

Where F is the strength, σ is the compressive stress, d_m is the matrix diameter, m_i = mass of the samples before the mechanical test, and m_f = mass of uncrushed samples after the mechanical test.

Friability was studied as described by Coelho et al. (2019) [51]. For this, 2 g of macrospheres were placed in a rotating drum (SOTAX/F1, Sotax Group, Germany), operating at 25 rpm for three cycles of 4 min each. After each cycle, the macrospheres were collected, weighed, and the results were presented as mass loss, according to Eq. (7).

2.6. In vitro cytocompatibility

Cellular cytotoxicity was evaluated according to ISO 10993-5 "Biological evaluation of medical devices – Part 5: Tests for *in vitro* cytotoxicity" [52] testing the macrospheres extracts. MC3T3-E1 pre-osteoblastic cells (CRL-2593, ATCC - Gibco) derived from mouse calvaria were cultured in alpha minimum essential medium (α-MEM) (Sigma-Aldrich) supplemented with 10 % (v/v) fetal bovine serum (FBS, Gibco) and 1 % (v/v) penicillin-streptomycin (p/s, Sigma-Aldrich) at 37 °C and 5 % CO_2. Cells were seeded on 96-well plates at a density of 1 × 10^5 cells.mL^{-1} and incubated for 24 h at 37 °C. The sample extracts were prepared according to ISO 10993-12 "Biological evaluation of medical devices - Part 12: Sample preparation and reference materials" [53]. The working volume was set at 100 μL. Macrospheres were sterilized by autoclaving at 120 °C for 20 min, then immersed in supplemented α-MEM with a fixed mass ratio to medium (0.2 g mL^{-1}) and incubated at 37 °C for 24 h and 5 % CO_2.

Cell metabolic activity was measured using the resazurin assay. The cell culture medium was removed, macrosphere extracts were centrifuged for 10 s, added to the cell culture, and incubated for 24 h at 37 °C and 5 % CO_2. The cytotoxic positive control was 1 % (v/v) Triton X-100 (Sigma-Aldrich), while only cells in α-MEM were used as the negative control. Without seeding, the blanks were only composed of the samples' extracts (or culture medium or 1 % (v/v) Triton for negative and positive controls, respectively). After 24, 48, and 72 h of incubation, the culture medium was discarded, and 10 % resazurin (v/v) in supplemented α-MEM was added to each well and incubated for 3 h at 37 °C and 5 % CO_2. After incubation, fluorescence was measured at 530 nm excitation and 590 nm emission in a Synergy MX fluorimeter (BioTek). Data were normalized relative to the negative control. Five samples per group were used in three independent assays.

The Live/Dead cell assay was also performed to evaluate cell viability by simultaneously quantifying live and dead cells. The live cells were stained with green-fluorescent calcein-AM (Thermo-Fisher), while dead cells were stained with red-fluorescent propidium iodide (PI - BD Biosciences). The cells were incubated with the sample extracts for one and three days at 37 °C and 5 % CO_2. The positive and negative controls consisted of cells incubated with 1 % (v/v) Triton X-100 with supplemented α-MEM, respectively. For each time point, culture medium was removed, 50 μL of calcein diluted in α-MEM (2 μL mL^{-1}), and 50 μL of PI diluted in phosphate buffer solution (PBS,50 %v/v) were added to each well and then incubated for 30 min at 37 °C and 5 % CO_2. After incubation, cells were visualized using an inverted fluorescence microscope (IFM, Zeiss, Germany) with green (488 nm) and red (594 nm) filters, and the acquired images were processed with ImageJ version 1.54 m.

2.7. Hemocompatibility

To assess the hemolytic potential of the macrospheres, sterilized samples (2 g mL^{-1}) by autoclave were incubated with human red blood cells (RBCs) according to ASTM F756:2017 "Standard Practice for Assessment of Hemolytic Properties of Materials" [54] and as described elsewhere [55]. Briefly, RBCs were extracted from human buffy coats (ethics protocol ref. [90]/19 with Hospital de São João, Porto, Portugal) by differential centrifugations at 400 G for 30 min. The upper layer was discarded, and the pellet (containing the RBCs) was diluted in PBS (1:400). The samples were incubated with isolated RBCs (4 × 10^8 cells. mL^{-1}) in a 48-well plate and incubated for 3 h at 37 °C. In addition, the

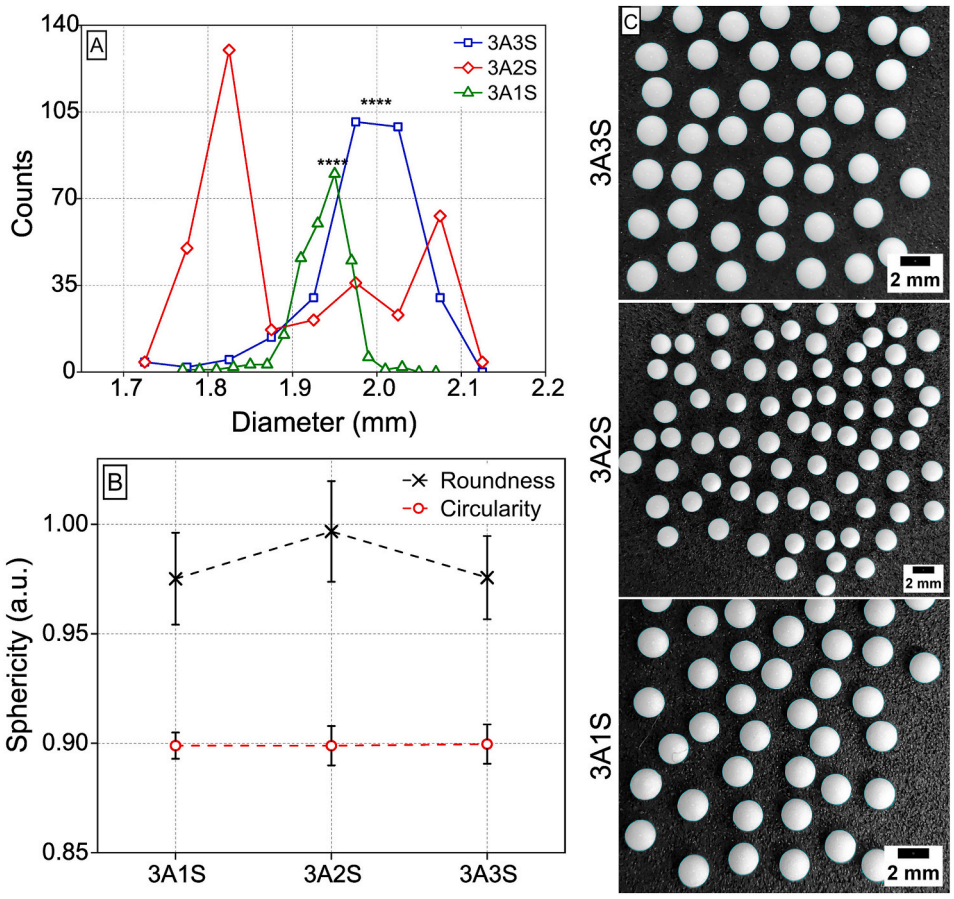

Fig. 7. (A) Particle size distribution. Symbols: 3A3S: blue □, 3A2S: red ◊, 3A1S: green Δ; (B) Sphericity parameters. Symbols: Roundness: black × , Circularity: red ○. Data are expressed as mean ± SD. Significant values****$p < 0.0001$ compared to 3A2S. (C) Original macrographs used in ImageJ analysis.

positive control (100 % hemolysis of RBCs) consisted of 1 % (v/v) Triton X-100 with RBCs, while the negative control was PBS mixed with RBCs. Following, the plate was centrifuged at 4000 rpm for 15 min, and 100 μL of the supernatant was collected for a 96-well plate to read the absorbance at 380, 415, and 450 nm using the SynergyMiX fluorimeter (BioTek). The amount of hemoglobin (HB) was calculated as the following Eq. (8):

$$HB\ (mg.dL^{-1}) = ((2 \times A415 - (A380 + A\ 450)) \times 100\ ) \ /\ E \quad (8)$$

A415, A380, and A450 represent the absorbance read at 415 nm, 380 nm, and 450 nm, respectively; E is the molar absorptivity of oxyhemoglobin at 450 nm.

The homolytic potential is determined by Eq. (9):

$$Hemolysis\ (\%) = RHsample\ /\ RHtotal \quad (9)$$

Where RHtotal is the amount of hemoglobin released in the positive control. Each assay was performed with five replicates.

2.8. In vitro proliferation

MC3T3-E1 Cells were cultured in α-MEM supplemented with 10 % (v/v) FBS and 1 % (v/v) p/s and incubated at 37 °C and 5 % CO_2. After cell confluence, cells were seeded on the macrospheres at 6×10^4 cells. cm^{-2}, and incubated for 3, 7, and 14 days at 37 °C and 5 % CO_2. Before seeding, samples were sterilized by autoclaving. Cells grown on the tissue culture plates (TCPS) without macrospheres were considered 100 % of cell viability or control [56].

Cellular metabolic activity was evaluated using the resazurin assay. After each time point, the culture medium was removed, and 10 % resazurin (v/v) was added to each well and incubated for 4 h. After incubation, the fluorescence was measured at an excitation of 530 and emission of 590 nm wavelengths in a SynergyMX fluorimeter (BioTek). Afterwards, the wells were cleaned with sterile PBS and loaded with fresh supplemented α-MEM. This test was performed using five samples (2 g mL^{-1}) for each macrosphere group in three independent assays. The results were expressed as relative fluorescent units (RFU). Furthermore, this assay was also performed using an osteogenic medium composed of supplemented α-MEM medium with 10 mM β-glycerophosphate, 0.01 mg mL^{-1} l-ascorbic acid, and 10^{-8} M dexamethasone.

The cultured samples were analyzed by confocal laser scanning microscopy (CLSM) and scanning electron microscopy (SEM) to observe cell morphology and adherence to the sample surfaces.

After 14 days of cell culture, the medium was discarded, and the samples were rinsed in non-sterile PBS. The samples were fixed with 4 % paraformaldehyde (Sigma-Aldrich) for 30 min, followed by incubation in 0.2 % (v/v) Triton X-100 solution (Sigma-Aldrich) for 10 min and 1 % (w/v) bovine serum albumin (BSA, Sigma-Aldrich) for 10 min. Cell cytoskeleton filamentous actin (F-actin) was stained with Alexa Fluor conjugated phalloidin 488 in 1 % BSA solution for 20 min at 50 rpm. Samples were washed twice with PBS, and nuclei were stained with DAPI (4′,6-diamidino-2-phenylindole) (0.5 μg mL^{-1}) for 20 min at 50 rpm. Samples were washed twice with PBS, and images of fluorescent-labeled cells were obtained using a confocal laser scanning microscope CLSM (TCS-SP5 AOBS, Leica microsystems) using 405 and 594 nm excitation lasers.

For SEM analysis, samples were fixed in 1.5 % (v/v) glutaraldehyde (diluted in 25 % cacodylate solution) for 15 min, followed by sequential dehydration in graded ethanol solutions (50 %, 70 %, 90 % and 100 % v/v) and hexamethyldisilane: ethanol (50 %, 70 %, 90 % and 100 % v/v,

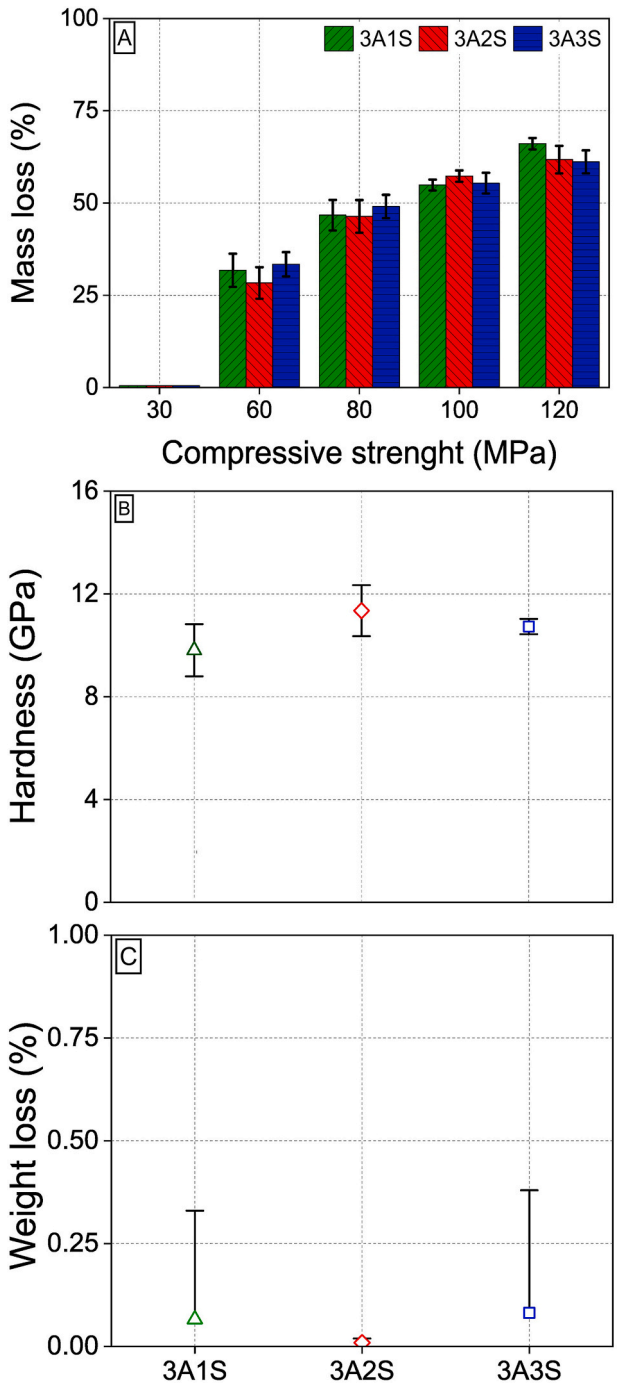

Fig. 8. Mechanical properties of alumina-silica macrospheres. Symbols 3A1S: green Δ, 3A2S: red ◊, 3A3S: blue □. (A) Mass loss (%) as a function of compressive strength (MPa). (B) Vickers microhardness (GPa). All samples presented high hardness, with slightly higher values for the 3A2S composition. (C) Mass loss (%) after friability test. Data are expressed as mean ± SD.

HMDS, Sigma-Aldrich) series. The samples were sputter-coated (Cressington Sputter Coater, 108 auto) with a 10 nm Au/Pd film for 1 min and observed by SEM (Nova NanoSEM 200 microscope, FEI), at 10 kV in SE mode.

2.9. Statistical analysis

All statistical analyses were performed using a One-Way analysis of variance (ANOVA) with GraphPad Prism version 5.02. Results are presented as mean ± standard deviation. Statistically significant differences were indicated with *p < 0.05, **p < 0.01 and ****p < 0.0001.

3. Results and discussion

3.1. Physicochemical characterization

The porosity results (Fig. 3) indicated low intra-sphere porosity (>20 %) in all compositions. The reduction in porosity with increasing colloidal silica content can be explained by improved packing as colloidal particles fill gaps that micrometric particles cannot reach [57,58], as observed in studies combining colloidal silica with other materials, such as MgO [59]. Furthermore, despite the low intra-sphere porosity (>20 %), due to their loose-fill format, high levels of inter-sphere porosity (40 %) can be achieved in all compositions, suggesting that the inter-sphere porosity was not directly related to the final composition of the synthesized compound or phases present ($Al_2O_3/Al_6Si_4O_{13}/SiO_2$). The advantages of using porous implants include enhanced nutrient transport, vascularization, and cell migration, as well as an increased contact area between the implant and the bone, which together contribute to improved osseointegration [2,5,60,61].

Porosity is a critical characteristic for cell adhesion and proliferation. The growth of osteoblastic cells has been reported in scaffolds with pore sizes ranging from 50 to 200 μm [62] -400 μm [63], and up to 600 μm [64], where nutrient transport is more effective in promoting metabolic activity and cell proliferation within macropores. In addition, the low fraction of closed porosity obtained by Archimedes' method indicates that most pore volume is accessible, thereby favoring an open pore network that supports fluid transport and nutrient diffusion, increasing the contact area between the implant and the bone, which is essential for cell migration and proliferation within the implant [36,61,65,66]. The ability to tailor intra-sphere porosity without compromising inter-sphere architecture represents a promising strategy for multifunctional design.

The type II typical N_2 adsorption isotherm (Fig. 4A) is typically observed in a non-porous or macroporous structure [67]. N_2 adsorption increased at high pressure, and when the adsorption and desorption curves do not coincide, hysteresis could occur during desorption [44], mainly in the case of aggregates with slit-shaped pores [67]. The 3A2S sample, in addition to higher specific surface area and total pore volume (Fig. 4B), showed a high absorbed volume, indicating a more open structure and greater pore accessibility. These results could suggest greater biological activity in this sample compared to 3A1S and 3A3S.

Thermogravimetric analysis (TGA) of the sodium alginate (SA) sphere is represented in Fig. 5A, showing the mass loss profile during heating. The initial weight loss below 150 °C is associated with the removal of physically adsorbed water [68]. The major mass-loss event between 200 and 300 °C corresponds to the thermal degradation of the sodium alginate [68,69].

DSC results revealed the reactions and phase transformations occurring during thermal treatment (Fig. 5B). An endothermic peak at 120 °C could be associated with the release of residual water, the burning of SA at 278 °C [70,71]. In line with the TGA results (Fig. 5A), the peak around 450 °C may be related to the dehydration and condensation of the silanol groups (forming Si–*O*–Si bonds and releasing water) [72] and the crystallization of SiO_2 can be associated with the 875 °C peak [73,74].

Dilatometric analysis (Fig. 5C) showed that all samples exhibit thermal shrinkage above 1200 °C, with shrinkage intensity varying according to silica content. Furthermore, the densification of the 3A3S sample at lower temperatures, possibly due to the glass transition temperature of SiO_2 (Tg, approximately 698 °C) [75–77], when particles became soft and deformable, or due to the formation of cristobalite at lower temperatures than mullite or Al_2O_3 sintering [74,78–81]. In all conditions, the differential thermal linear variation was interrupted around 1500 °C. It is known that the densification of mullite ceramics

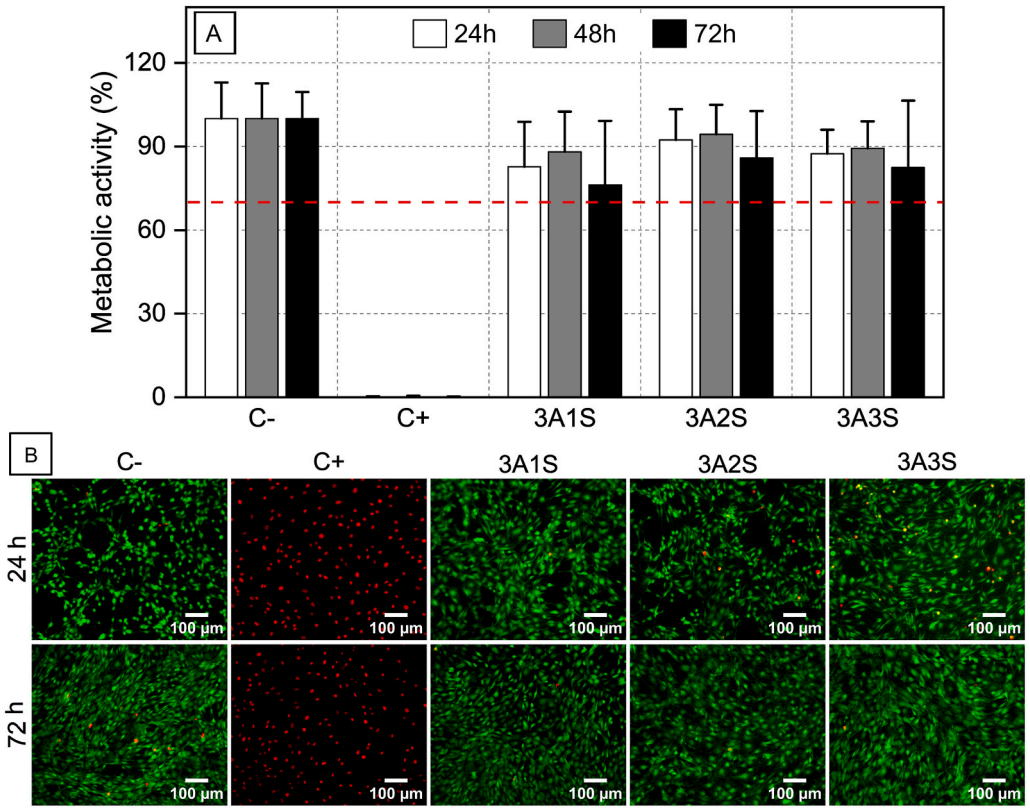

Fig. 9. Cell viability of MC3T3-E1 cells. (A) Metabolic activity over time with the sample extracts for different groups: C^- (negative control), C^+ (positive control), 3A1S, 3A2S, 3A3S (experimental samples); red dashed line indicates 70 % cell viability according to ISO 10993. White bars correspond to 24 h, grey bars to 48 h, and black bars to 72 h of incubation. Data are expressed as mean ± SD. (B) Live/Dead cell viability staining after 24 and 72 h. The color green corresponds to living cells (stained with calcein) and the color red to dead cells (stained with propidium iodide). Scale bar: 100 µm.

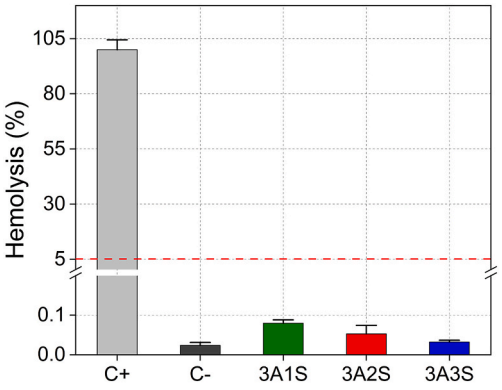

Fig. 10. Hemolysis activity of alumina-silica macrospheres after exposure to red blood cells. C^+ (positive control, LT grey bay): 1 % Triton; C^- (negative control, grey bar): PBS; 3A1S (green bar), 3A2S (red bar), 3A3S (blue bar): experimental samples. The red dashed line at 5 % indicates hemocompatibility according to ASTM F756:2017 standard. Data are expressed as mean ± SD.

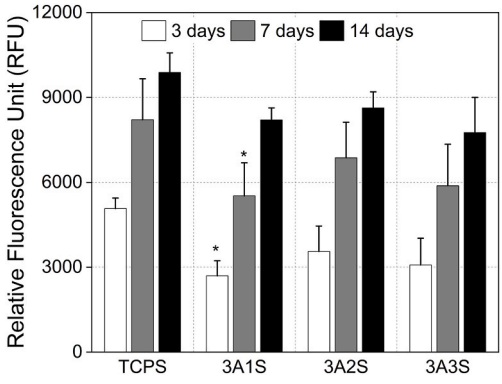

Fig. 11. Cell metabolic activity of MC3T3 cultured on alumina-silica macrospheres over a 14-day culture period. TCPS (control): PBS; 3A1S, 3A2S, 3A3S: experimental compositions. White bars correspond to 3, grey bars to 7, and black bars to 14 days of incubation. An increase in fluorescence intensity over time indicates progressive cell adhesion and proliferation on all compositions. Data are expressed as mean ± SD. *p ≤ 0.05 comparing to 3A2S.

occurs at temperatures around 1600 °C [82,83] by a liquid phase formation; however, the use of colloidal precursors, as colloidal silica, can decrease the sintering temperature [44,84].

The phase composition of the alumina-silica macrospheres sintered at 1500 °C is represented in Fig. 6A. In the XRD diffractograms of the sintered samplesthe identified phases corresponded to alumina (A, JPCDS 1–1243), cristobalite (C, JCPDS 1–438), and mullite (M, JCPDS 1–163). The mullite *in situ* is reported at lower temperatures for systems with other SiO_2 sources [82,84,85]. However, cristobalite formation can occur at low temperatures [74,86], consuming the SiO_2 available to react with Al_2O_3 at higher temperatures. This may have contributed to the simultaneous production of the three phases. The biocompatibility of all these phases supports the potential use of these samples in biomedical implants [27,42,43].

The FTIR spectra (Fig. 6B) analysis confirmed the formation of aluminosilicate structures, consistent with mullite development. In more detail, the bands referred to stretching and bending of adsorbed water and hydroxyl groups were identified at 3420 and 1632 cm^{-1} [87–89]. The peaks at 1170 and 648 cm^{-1} correspond to Si–*O*–Al [87],

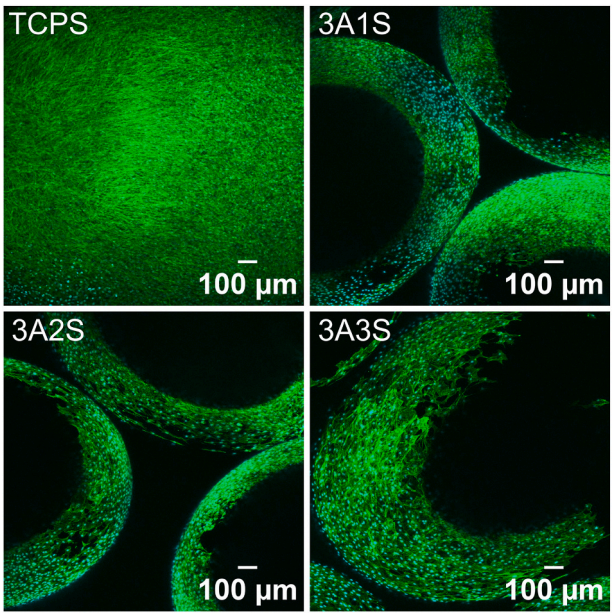

Fig. 12. Cell adhesion on the surface of the TCPS, 3A1S, 3A2S, 3A3S after 14 days. The color green corresponds to cell cytoskeleton actin (stained with Alexa Fluor and phalloidin), and the color blue corresponds to cell nuclei (stained with DAPI). The green fluorescence signal indicates viable adherent cells, demonstrating successful cell attachment and spreading. Scale bar: 100 µm.

and at 1110 cm^{-1} to the asymmetric stretch of Si–*O*–Si of the SiO_2 [88,90]. The band at 1385 cm^{-1} has been identified as Al–O bonds in Al_2O_3 [89], at 825 and 735 cm^{-1} as tetrahedral Al–O [38]. Finally, the peaks at 570 and 468 cm^{-1} were attributed to Al–O vibration modes resulting from AlO_6 mullite groups [88,90].

The silanol groups (Figs. 5B and 6B) are essential for hydroxyapatite nucleation in contact with body fluids, thereby forming a bioactive layer on the biomaterial surface that mimics the mineral composition of human bone [31,91–93]. This layer will promote an integration between the implant and native bone, providing an interface that stimulates bone regeneration [91,94–96]. Furthermore, Si–OH acts directly on the absorption of proteins by cells, which can promote their proliferation and differentiation [97,98], thus improving mineralization, new bone formation, and contributing to implant regeneration and integration [99,100].

3.2. Morphological properties

The particle size distribution (Fig. 7A) and sphericity (roundness and circularity, Fig. 7B) of alumina-silica macrospheres were determined by ImageJ analysis from the corresponding macrographs (Fig. 7C). There was a wide range in diameter distribution after sintering, particularly for the 3A2S condition (Fig. 7A), which was reduced for the 3A1S and 3A3S compositions. This distribution has been observed in studies of bioglass spheres produced by the same technique [21]. Comparing the average diameters obtained in the 3A2S sample with those in the others, it was found that the 3A2S sample was statistically different. This may have occurred due to the difference in the production of the cristobalite and mullite phases at high temperatures (Fig. 6). Obtaining mullite *in situ* generally has an expansive character due to its low solid density (3.2 g cm^{-3}) compared to alumina (4.0 g cm^{-3}), and the shrinkage or densification is improved [101,102] with the increase in the amount of SiO_2 available in the system (Fig. 5C). The sphericity values range from 0.00 to 1.00, with 1.00 indicating a perfect sphere. Sphericity was assessed by circularity and roundness (Fig. 7B), and the samples did not show statistical differences, as all samples exhibited a circularity of approximately 0.90 ± 0.02 and roundness ranging from 0.97 to 0.99, indicating their nearly perfect sphericity. Alumina spheres fabricated by the same technique presented similar sphericity [103]. Optimal sphericity values improve packing, generating an interconnected macroporosity between spheres that could support nutrient transport and cell growth across the implant [21,25].

3.3. Mechanical characterization

The compressive strength of the spheres was evaluated by their resistance to mass loss under increasing mechanical stress. At 30 MPa, all formulations retained complete structural integrity, with zero mass loss observed (Fig. 8A). Mass loss increased as stress increased, reaching 70 % at 120 MPa. It is important to note that the compressive performance of the samples aligns with biological benchmarks: human cortical bone can withstand compressive strengths of 150 MPa, whereas cancellous bone supports around 20 MPa [27,100,104]. Therefore, Al_2O_3–SiO_2 spheres could be tailored for use at different anatomical sites, depending on the mechanical demands of the implantation site.

Vickers hardness testing is widely used for characterizing biomaterials due to its suitability for evaluating thin components and fine microstructures. This method can estimate the degree of mineralization and overall quality of bone tissue, which often varies depending on anatomical site and bone size [105,106]. Additionally, it enables direct comparison of the mechanical properties of synthetic materials with those of native bone tissue. In this study, all Al_2O_3–SiO_2 bioceramic spheres presented a hardness of approximately 10 GPa (Fig. 8B), with the 3A2S sample exhibiting the highest value, followed by 3A3S and 3A1S. These values are in agreement with previously reported data for mullite-based ceramics sintered at approximately 1500 °C [107,108]. The high hardness values observed here suggest that the materials are suitable for applications requiring wear resistance and mechanical durability. Additionally, the weight loss remained below 1 % for all samples (Fig. 8C), indicating good wear resistance in the loose-fill application.

3.4. In vitro cytocompatibility

Biocompatibility is a critical characteristic of macrospheres used as bone grafts, as it ensures that the material integrates with the body without causing adverse effects. According to the ISO 10993-5 standard [52], cell viability above 70 % is considered non-cytotoxic. The cytocompatibility of the experimental samples was assessed using a quantitative cell viability assay and qualitative live/dead cell imaging (Fig. 9). At all evaluated time points, negative control (C^-) maintained high viability (>95 %), confirming normal cell growth (Fig. 9A). The positive control (C^+) exhibited cytotoxicity, with viability below 1 %. The macrospheres were cytocompatible, exhibiting cell viability above 90 % under all tested conditions, even after 72 h of exposure (Fig. 9B), indicating that the materials do not induce cytotoxicity effects [25,56]. Although no significant deviations were observed, slight differences in cell viability were noted among 3A1S, 3A2S, and 3A3S, which may be attributed to variations in formulation and surface characteristics. Complementing this, samples showed no statistical differences compared to the C^-, indicating that the material did not inhibit cell activity, even with increasing incubation time. The Live/Dead images supported these findings, revealing a predominance of live cells across all experimental groups (Fig. 9B), exhibiting a similar behavior to the C^-. Furthermore, cell density increased with incubation time, showing that the material does not impede cell growth, as observed with biocompatible materials [51]. Given these results, the produced macropheres showed promising biocompatibility for use in bone tissue engineering.

3.5. Hemocompatibility

The hemolytic potential of the materials was evaluated to assess their

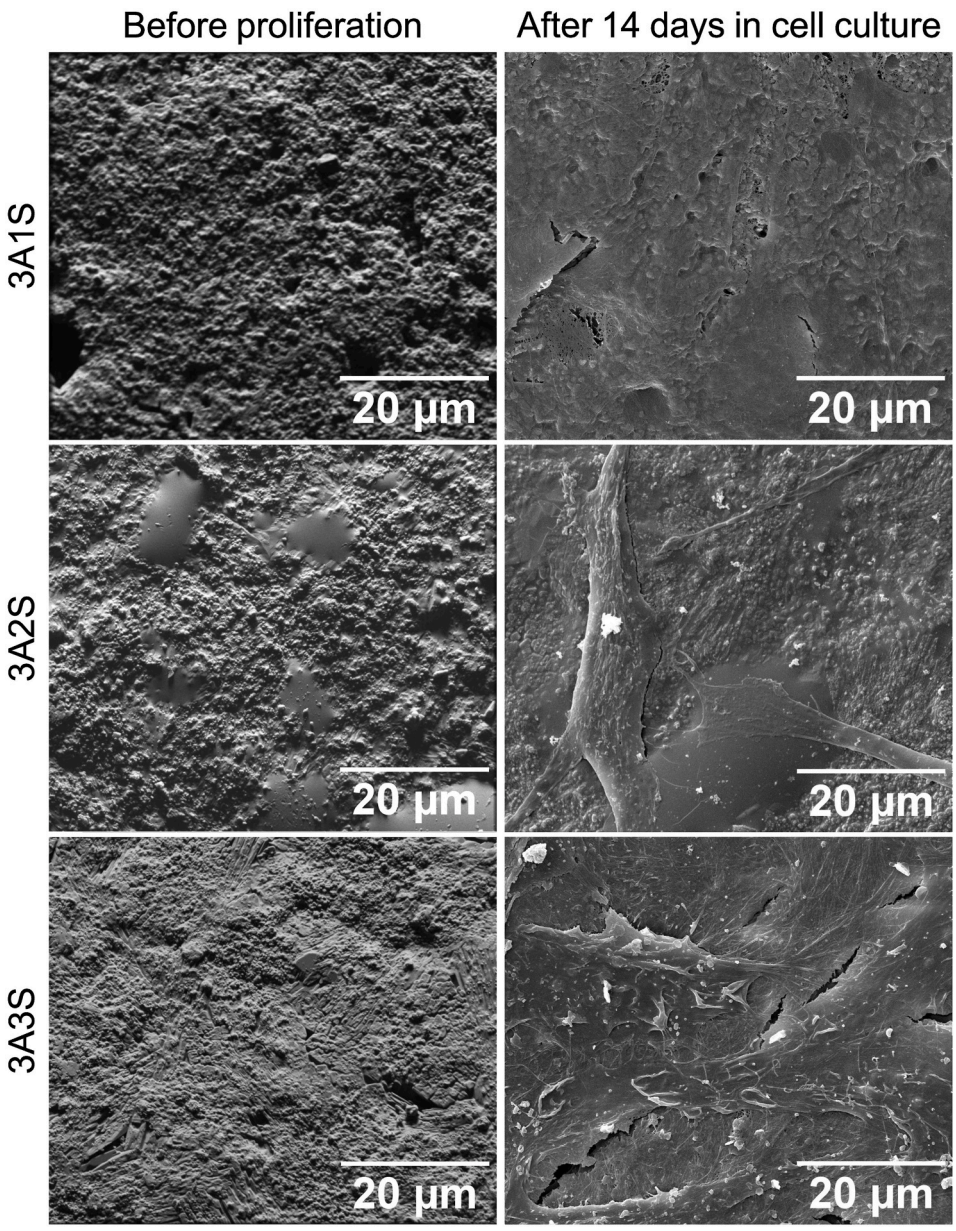

Fig. 13. SEM micrographs of alumina-silica macrospheres before cell seeding (left) and after 21 days of MC3T3 culture (right). Post-culture images show adhered and spread cells with extracellular matrix formation across the surface. Scale bar: 20 μm.

blood compatibility, which is critical for applications involving direct blood contact [55,109]. According to the ASTM F756:2017 standard [54], a material is considered non-hemolytic if hemolysis is below 5 %. All experimental conditions demonstrated minimal hemolytic activity (<0.1 %) (Fig. 10) and did not differ statistically from the C^+ condition, indicating that the Al_2O_3–SiO_2 macrospheres did not affect red blood cell integrity being classified as hemocompatible.

3.6. *In vitro* proliferation

To evaluate the *in vitro* cell proliferation, MC3T3-E3 cells were seeded on the microsphere samples and cultured for 14 days. At day 3, cell proliferation on all ceramic samples was lower than on the control (TCPS), although the differences were not statistically significant (Fig. 11). However, on day 7, a substantial increase in metabolic activity was observed across all groups, indicating that cell proliferation was not affected, even in direct contact with the material. Comparing the influence of the macrospheres' composition, a statistical difference was only observed between the 3A2S and 3A1S conditions at the initial time (3 days), but this difference was not sustained after 14 days. Thus, the Al_2O_3–SiO_2 ratio in the composition of the macrospheres did not exert the most significant influence on metabolic activity with increasing incubation time.

Confocal laser scanning microscopy was used to qualitatively assess cell adhesion and spatial distribution on the surface after *in vitro* culture. The cells adhered to the entire surface of the spheres (Fig. 12). A higher cell density is observed in the contact area between the spheres, suggesting that tissue regeneration occurs primarily at the porosity between them.

The surface morphology of the samples was observed using scanning electron microscopy (SEM) before cell seeding and after 14 days of *in vitro* culture (Fig. 13). Before proliferation, all samples exhibited distinct microstructures. The 3A1S surface exhibited high roughness and open pores, which may initially improve cell attachment [110]. The 3A2S surface displayed a slightly smoother texture, which may facilitate initial cell anchorage [42]. In contrast, 3A3S showed a more textured

surface with elongated crystalline structures, potentially enhancing cell–material interaction. After 2 days of culture, all samples showed evidence of cellular attachment and extracellular matrix formation. In 3A1S, the surface appeared covered by a cellular layer, similar to that observed in other studies [25,36]. In 3A2S, a more defined cell morphology was observed, suggesting active interaction between cells and the substrate, and the 3A3S surface was extensively covered with a dense cellular layer and abundant osteoblastic-like structures, indicating robust cell proliferation [42,111,112].

4. Conclusions

Al_2O_3–SiO_2 ceramic macrospheres with different chemical compositions were produced by ionotropic gelcasting. Thermal treatment led to the formation of biologically favorable crystalline phases, including mullite and cristobalite. All compositions had good sphericity (circularity ~0.90 and roundness ~0.97), which allowed for easier packing and the formation of inter-sphere macroporosity (~40 %). The presence of silanol groups (Si–OH) can induce the formation of a bioactive surface, facilitating direct integration with native bone tissue, thereby enhancing osseointegration and stimulating osteoblastic activity. The mechanical properties, including high Vickers hardness (~10 GPa) and compressive resistance up to 120 MPa, meet the requirements of cancellous and some cortical bone regions, ensuring that the spheres can maintain structural integrity under physiological loads. *In vitro* biological evaluations confirmed the cytocompatibility and hemocompatibility of the material, as well as its ability to support cell adhesion, and proliferation. Among the three compositions, the stoichiometric mullite, sample 3A2S ($3Al_2O_3{\cdot}2SiO_2$), exhibited the most balanced combination of mechanical strength (improved compressive strength and hardness without excessive densification), specific surface area (more surface available for protein adsorption and cell interaction), and biocompatibility (good metabolic activity, cyto and hemocompatibility). Overall, these findings indicate that Al_2O_3–SiO_2 macrospheres combine structural, chemical, and biological properties that are synergistic with the demands of bone tissue regeneration. This supports their usage as injectable or granular materials for defect repair in orthopedic and dental applications.

Declaration of competing interest

The authors declare that they have no known competing financial interests or personal relationships that could have appeared to influence the work reported in this paper.

Acknowledgments

The authors acknowledge Brazilian Research Foundations CNPq (140930/2022-1), FAPESP, CAPES (001), FCT – Fundação para a Ciência e a Tecnologia, Portugal, for financial support (PhD grant 2021.07672. BD) and under the project https://doi.org/10.54499/2021.07672.BD, Nouryon South America (Brazil) and Almatis (US and Brazil) for kindly supplying samples of colloidal silica and calcined alumina. The authors thank Fundação de Ciência e Tecnologia (FCT) for supporting the Junior Researcher Grants (https://doi.org/10.54499/2022.05157.CEECIND/CP1735/CT0011) and (https://doi.org/10.54499/2023.08230.CEECIND/CP2844/CT0008), and HfPT - Health from Portugal project [C630926586-00465198 | Projeto n° 41], co-financed by the PRR - Programa de Recuperação e Resiliência, within the scope of Next Generation from the European Union (https://recuperarportugal.gov.pt/).

References

[1] Ribeiro AA, Balbuena OBF, Lima AM, de Souza Alves L, Monteiro MM, de Oliveira MV, Pereira LC. Effect investigation of ammonium bicarbonate and polyethylene wax as pore-forming agents on the physicochemical properties of macroporous biphasic calcium phosphate bioceramics processed by space-holder technique. Mater Res 2024;27. https://doi.org/10.1590/1980-5373-MR-2024-0270.

[2] Nath S, Basu B, Mohanty M, Mohanan PV. In vivo response of novel calcium phosphate-mullite composites: results up to 12 weeks of implantation. J Biomed Mater Res B Appl Biomater 2009;90 B:547–57. https://doi.org/10.1002/jbm.b.31316.

[3] Mofakhami S, Salahinejad E. Biphasic calcium phosphate microspheres in biomedical applications. J Contr Release 2021;338:527–36. https://doi.org/10.1016/j.jconrel.2021.09.004.

[4] Tavares MT, Oliveira MB, Mano JF, Farinha JPS, Baleizão C. Bioactive silica nanoparticles with calcium and phosphate for single dose osteogenic differentiation. Mater Sci Eng C 2020;107. https://doi.org/10.1016/j.msec.2019.110348.

[5] Sartori TAI, Ferreira JA, Osiro D, Colnago LA, de EM, Pallone JA. Formation of different calcium phosphate phases on the surface of porous Al2O3-ZrO2 nanocomposites. J Eur Ceram Soc 2018;38:743–51. https://doi.org/10.1016/j.jeurceramsoc.2017.09.014.

[6] Duraccio D, Strongone V, Malucelli G, Auriemma F, De Rosa C, Mussano FD, Genova T, Faga MG. The role of alumina-zirconia loading on the mechanical and biological properties of UHMWPE for biomedical applications. Compos B Eng 2019;164:800–8. https://doi.org/10.1016/j.compositesb.2019.01.097.

[7] Bagherivand A, Jafarirad S, Norouzi R, Karimi A. Biomedical behaviors of CuO/γ-alumina/chitosan nanocomposites: scolicidal and apoptotic effects on hydatid cysts protoscolices. Int J Biol Macromol 2024;263. https://doi.org/10.1016/j.ijbiomac.2024.130515.

[8] Ruys A. Introduction to alumina ceramics. https://doi.org/10.1016/b978-0-08-102442-3.00001-4; 2019.

[9] Andreto CG, Rodarte M, Balestra RM, Alves LS, Ribeiro AA, Monteiro M. Biomimetic coating of Alumina scaffolds at different imersion times. Revista Sociedad Científica Del Paraguay 2025;30:45–55. https://doi.org/10.32480/rscp.2025.30.1.4455.

[10] Morks MF, Kobayashi A. Development of ZrO2/SiO2 bioinert ceramic coatings for biomedical application. J Mech Behav Biomed Mater 2008;1:165–71. https://doi.org/10.1016/j.jmbbm.2007.09.002.

[11] Toloue EB, Karbasi S, Salehi H, Rafienia M. Potential of an electrospun composite scaffold of poly (3-hydroxybutyrate)-chitosan/alumina nanowires in bone tissue engineering applications. Mater Sci Eng C 2019;99:1075–91. https://doi.org/10.1016/j.msec.2019.02.062.

[12] Li X, Shi J, Zhu Y, Shen W, Li H, Liang J, Gao J. A template route to the preparation of mesoporous amorphous calcium silicate with high in vitro bone-forming bioactivity. J Biomed Mater Res B Appl Biomater 2007;83:431–9. https://doi.org/10.1002/jbm.b.30813.

[13] Zhang J, Zhu Y, Li J, Zhu M, Tao C, Hanagata N. Preparation and characterization of multifunctional magnetic mesoporous calcium silicate materials. Sci Technol Adv Mater 2013;14. https://doi.org/10.1088/1468-6996/14/5/055009.

[14] Ismail H, 'Atiqah Abdul Azam F, Zainuddin Z, Bunawan H, Akbar MA, Mohamad H, Hamid MAA. Effects of mullite, maghemite, and silver nanoparticles incorporated in β-wollastonite on tensile strength, magnetism, bioactivity, and antimicrobial activity. Materials 2021;14. https://doi.org/10.3390/ma14164643.

[15] Hernández Montoto A, Llopis-Lorente A, Gorbe M, Terrés JM, Cao-Milán R, Díaz de Greñu B, Alfonso M, Ibañez J, Marcos MD, Orzáez M, Villalonga R, Martínez-Máñez R, Sancenón F. Janus gold nanostars–mesoporous silica nanoparticles for NIR-Light-Triggered drug delivery. Chem Eur J 2019;25:8471–8. https://doi.org/10.1002/chem.201900750.

[16] Tajuddin MF, Al-Gheethi A, Mohamed R, Noman E, Talip BA, Bakar A. Optimizing of heavy metals removal from car wash wastewater by chitosan-ceramic beads using response surface methodology. Mater Today Proc 2020;31:43–7. https://doi.org/10.1016/j.matpr.2020.01.085.

[17] Han XY, Zhao DL, Meng WJ, Yang HX, Wu YQ, Gao RZ, Yang Y, Pu H. Hollow tremella-like graphene sphere/SnO2 composite for high performance Li-ion battery anodes. Ceram Int 2019;45:16244–50. https://doi.org/10.1016/j.ceramint.2019.05.146.

[18] Mishra A, Melo JS, Bhainsa KC. Application of conventional spray dryer to prepare nanosilica-alginate based rhodamine loaded microstructures and nanobeads. J Mater Res 2023;38:3362–71. https://doi.org/10.1557/s43578-023-01056-z.

[19] Mishra A, Pandey VK, Shankar BS, Melo JS. Spray drying as an efficient route for synthesis of silica nanoparticles-sodium alginate biohybrid drug carrier of doxorubicin. Colloids Surf B Biointerfaces 2021;197:111445. https://doi.org/10.1016/j.colsurfb.2020.111445.

[20] Han L, Dong L, Li F, Duan H, Zhang H, Li G, Jia Q, Zhang S. Preparation of Si3N4-BCxN-TiN composite ceramic aerogels via foam-gelcasting. J Eur Ceram Soc 2022;42:2699–706. https://doi.org/10.1016/j.jeurceramsoc.2022.01.059.

[21] Oliveira IR, Gonçalves I dos S, Kennedy W dos S, Lança MC, Vieira T, Silva JC, Cengiz IF, Reis RL, Oliveira JM, Borges JPMR. Biocomposite macrospheres based on strontium-bioactive glass for application as bone fillers. ACS Mater Au 2023. https://doi.org/10.1021/acsmaterialsau.3c00048.

[22] Salomão R, Poiani AJB, Costa LMM. Porous beads of in-situ calcium hexaluminate prepared by extrusion-dripping. Interceram: International Ceramic Review 2019;68:40–9. https://doi.org/10.1007/s42411-019-0006-y.

[23] Lee HJ, Jeon JH, Kim CH, Kim YJ. Photosynthetic microporous bioactive glass ceramic beads for treating avascular osteonecrosis. J Ind Eng Chem 2023;122:551–61. https://doi.org/10.1016/j.jiec.2023.03.019.

[24] Soury R, Jabli M, Latif S, Alenezi KM, El Oudi M, Abdulaziz F, Teka S, El Moll H, Haque A. Synthesis and characterization of a new meso-tetrakis (2,4,6-trimethylphenyl) porphyrinto) zinc(II) supported sodium alginate gel beads for improved adsorption of methylene blue dye. Int J Biol Macromol 2022;202:161–76. https://doi.org/10.1016/j.ijbiomac.2022.01.087.
[25] Coelho CC, Padrão T, Costa L, Pinto MT, Costa PC, Domingues VF, Quadros PA, Monteiro FJ, Sousa SR. The antibacterial and angiogenic effect of magnesium oxide in a hydroxyapatite bone substitute. Sci Rep 2020;10. https://doi.org/10.1038/s41598-020-76063-9.
[26] Sepulveda P. Gelcasting foams for porous ceramics. Am Ceram Soc Bull 1997;76:61–5.
[27] Hench LL. An introduction to bioceramics. second ed. London: Imperial College Press; 2013.
[28] Salomão R. Porogenic behavior of water in high-alumina castable structures. Adv Mater Sci Eng 2018;2018. https://doi.org/10.1155/2018/2876851.
[29] Salomão R, Cardoso PH, Brandi J. Gelcasting porous alumina beads of tailored shape and porosity. Ceram Int 2014;40:16595–601. https://doi.org/10.1016/j.ceramint.2014.08.017.
[30] Ahmed MK, Ramadan R, Afifi M, Menazea AA. Au-doped carbonated hydroxyapatite sputtered on alumina scaffolds via pulsed laser deposition for biomedical applications. J Mater Res Technol 2020;9:8854–66. https://doi.org/10.1016/j.jmrt.2020.06.006.
[31] Yetri Y, Ikhsan, Indra A, Affi J. Gunawarman, Extraction of hydroxyapatite from bovine bones: the manufacturing development and its behavior properties towards acrylic resin/hydroxyapatite/alumina composites. Mater Chem Phys 2024;319. https://doi.org/10.1016/j.matchemphys.2024.129244.
[32] Camilo CC, Fortulan CA, Ikegami RA, R SJA, De M PB. Manufacturing of porous elumina scaffolds with bio-glass and HAp coating: mechanical and in vitro evaluation. Key Eng Mater 2009;396–398:679–82. https://doi.org/10.4028/0-87849-353-0.679.
[33] Kido HW, Ribeiro DA, De Oliveira P, Parizotto NA, Camilo CC, Fortulan CA, Marcantonio E, Da Silva VHP, Muniz Renno AC. Biocompatibility of a porous alumina ceramic scaffold coated with hydroxyapatite and bioglass. J Biomed Mater Res 2014;102:2072–8. https://doi.org/10.1002/jbm.a.34877.
[34] Mahmoodiyan Najafabadi F, Karbasi S, Zamanlui Benisi S, Shojaei S, Poursamar SA, Nasr Azadani R. Evaluation of the effects of alumina nanowire on 3D printed polycaprocactone/magnetic mesoporous bioactive glass scaffold for bone tissue engineering applications. Mater Chem Phys 2023;303:127616. https://doi.org/10.1016/j.matchemphys.2023.127616.
[35] Araujo MS, Silva AC, Cabal B, Bartolomé JF, Mello-Castanho S. In vitro bioactivity and antibacterial capacity of 45S5 bioglass®-based compositions containing alumina and strontium. J Mater Res Technol 2021;13:154–61. https://doi.org/10.1016/j.jmrt.2021.04.053.
[36] Ghafari F, Karbasi S, Eslaminejad MB. Investigating of physical, mechanical, and biological properties of polyhydroxybutyrate-keratin/alumina electrospun scaffold utilized in bone tissue engineering. Mater Chem Phys 2023;297:127340. https://doi.org/10.1016/j.matchemphys.2023.127340.
[37] Flores M, Ribeiro TP, Madureira S, Skwira-Rucińska A, Pinto MT, Monteiro FJ, Laranjeira MS. Development of a magnetic biomimetic scaffold for improved bone regeneration via static magnetic stimulation. Ceram Int 2025;51:7519–26. https://doi.org/10.1016/j.ceramint.2024.12.188.
[38] Zafar B, Mottaghitalab F, Shahosseini Z, Negahdari B, Farokhi M. Silk fibroin/alumina nanoparticle scaffold using for osteogenic differentiation of rabbit adipose-derived stem cells. Materialia 2020;9. https://doi.org/10.1016/j.mtla.2019.100518.
[39] Ribeiro T, Raja S, Rodrigues AS, Fernandes F, Baleizão C, Farinha JPS. NIR and visible perylenediimide-silica nanoparticles for laser scanning bioimaging. Dyes Pigments 2014;110:227–34. https://doi.org/10.1016/j.dyepig.2014.03.026.
[40] Jeelani PG, Mulay P, Venkat R, Ramalingam C. Multifaceted application of Silica nanoparticles. A review. Silicon 2020;12:1337–54. https://doi.org/10.1007/s12633-019-00229-y.
[41] Yang F, Zhao S, Chen G, Li K, Fei Z, Mummery P, Yang Z. High-strength, multifunctional and 3D printable mullite-based porous ceramics with a controllable shell-pore structure. Adv Powder Mater 2024;3. https://doi.org/10.1016/j.apmate.2023.100153.
[42] Fernandes L, De Carvalho RA, Amaral AC, Pecoraro E, Salomão R, Trovatti E. Mullite cytotoxicity and cell adhesion studies. J Mater Res Technol 2019;8:2565–72. https://doi.org/10.1016/j.jmrt.2019.04.001.
[43] Yetmez M, Erkmen ZE, Kalkandelen C, Ficai A, Oktar FN. Sintering effects of mullite-doping on mechanical properties of bovine hydroxyapatite. Mater Sci Eng C 2017;77:470–5. https://doi.org/10.1016/j.msec.2017.03.290.
[44] Bagchi B, Dey S, Bhandary S, Das S, Bhattacharya A, Basu R, Nandy P. Antimicrobial efficacy and biocompatibility study of copper nanoparticle adsorbed mullite aggregates. Mater Sci Eng C 2012;32:1897–905. https://doi.org/10.1016/j.msec.2012.05.011.
[45] Dubey AK, Sitesh G, Nath S, Basu B. Spark plasma sintering to restrict sintering reactions and enhance properties of hydroxyapatite-mullite biocomposites. Ceram Int 2011;37:2755–61. https://doi.org/10.1016/j.ceramint.2011.04.032.
[46] ASTM C1069-09. Test method for specific surface area of Alumina or quartz by nitrogen adsorption. West Conshohocken, PA: ASTM International; 2022. https://doi.org/10.1520/C1069-09R22.
[47] Aramaki S, Roy R. Revised phase diagram for the System Al2O3—SiO2. J Am Ceram Soc 1962;45:229–42. https://doi.org/10.1111/j.1151-2916.1962.tb11133.x.
[48] ASTM B962-23. Test methods for density of compacted or sintered Powder petallurgy (PM) products using archimedes principle. ASTM International; 2023. https://doi.org/10.1520/B0962-23.
[49] ASTM C 1327-15. Standard Test method for vickers indentation hardness of advanced ceramics. www.astm.org; 2019.
[50] NBR ISO 13503-2. Petroleum and natural gas industries-Completion fluids and materials tart 2: measurement of properties of proppants used in hydraulic fracturing and gravel-packing operations. www.abnt.org.br; 2011.
[51] Coelho CC, Araújo R, Quadros PA, Sousa SR, Monteiro FJ. Antibacterial bone substitute of hydroxyapatite and magnesium oxide to prevent dental and orthopaedic infections. Mater Sci Eng C 2019;97:529–38. https://doi.org/10.1016/j.msec.2018.12.059.
[52] ISO 10993-5. Biological evaluation of medical devices- part 5: tests for in vitro cytotoxicity. 2009.
[53] ISO 10993-12. Biological evaluation of medical devices - part 12: sample preparation and reference materials. www.abnt.org.br; 2005.
[54] ASTM F756-17. Standard practice for assessment of hemolytic properties of materials. West Conshohocken, PA: ASTM International; 2017. https://doi.org/10.1520/F0756-13.
[55] Moura D, Pereira AT, Ferreira HP, Barrias CC, Magalhães FD, Bergmeister H, Gonçalves IC. Poly(2-hydroxyethyl methacrylate) hydrogels containing graphene-based materials for blood-contacting applications: from soft inert to strong degradable material. Acta Biomater 2023;164:253–68. https://doi.org/10.1016/j.actbio.2023.04.031.
[56] Salgado CL, Mansur AAP, Mansur HS, Monteiro FJM. Bioengineered fluorescent nanoprobe conjugates for tracking human bone cells: in vitro biocompatibility analysis. Materials 2021;14. https://doi.org/10.3390/ma14164422.
[57] Oliveira IR, Studart AR, Pileggi RG, Pandofelli VC. Dispersão e Empacotamento de Partículas: princípios e Aplicações em Processamento Cerâmico, São Paulo. https://doi.org/10.1177/1748895811401979; 2000.
[58] McGeary RK. Mechanical packing of spherical particles. J Am Ceram Soc 1961;44:513–22. https://doi.org/10.1111/j.1151-2916.1961.tb13716.x.
[59] Salomão R, Martinatti IS, Fernandes L, Sundblom A, Tiba PRT. Colloidal silica as an anti-hydroxylation binder for pressed MgO structures. J Eur Ceram Soc 2025;45. https://doi.org/10.1016/j.jeurceramsoc.2025.117517.
[60] Deb P, Barua E, Deoghare AB, Das Lala S. Development of bone scaffold using Puntius conchonius fish scale derived hydroxyapatite: physico-pechanical and bioactivity evaluations. Ceram Int 2019;45:10004–12. https://doi.org/10.1016/j.ceramint.2019.02.044.
[61] Ren X, Tuo Q, Tian K, Huang G, Li J, Xu T, Lv X, Wu J, Chen Z, Weng J, Wang Q, Mu Y. Enhancement of osteogenesis using a novel porous hydroxyapatite scaffold in vivo and vitro. Ceram Int 2018;44:21656–65. https://doi.org/10.1016/j.ceramint.2018.08.249.
[62] Chen X, Gao CY, Chu XY, Zheng CY, Luan YY, He X, Yang K, Zhang DL. VEGF-Loaded heparinised gelatine-hydroxyapatite-tricalcium phosphate scaffold accelerates bone regeneration via enhancing osteogenesis-angiogenesis coupling. Front Bioeng Biotechnol 2022;10. https://doi.org/10.3389/fbioe.2022.915181.
[63] Oh SH, Park IK, Kim JM, Lee JH. In vitro and in vivo characteristics of PCL scaffolds with pore size gradient fabricated by a centrifugation method. Biomaterials 2007;28:1664–71. https://doi.org/10.1016/j.biomaterials.2006.11.024.
[64] Gu Y, Liu Y, Jacobs R, Wei L, Sun Y, Tian L, Liu Y, Politis C. BMP-2 incorporated into a biomimetic coating on 3D-printed titanium scaffold promotes mandibular bicortical bone formation in a beagle dog model. Mater Des 2023;228:111849. https://doi.org/10.1016/j.matdes.2023.111849.
[65] Swain S, Swain P, Parida SK, Rautray TR. Ceramic scaffolds for biomaterials applications. In: Advanced ceramic coatings for biomedical applications. Elsevier; 2023. p. 223–48. https://doi.org/10.1016/B978-0-323-99626-6.00016-0.
[66] Cai Y, Sun X, Feng Q, Li B, Li X, Chen S, Zhou X, He C. Self-adaptive bioactive scaffolds orchestrate diabetic microenvironment remodeling and vascularized bone regeneration. Compos B Eng 2024:111771. https://doi.org/10.1016/j.compositesb.2024.111771.
[67] Sing KSW, Everett DH, Haul RAW, Moscou L, Perotti RA, Rouquérol J, Siemieniewska T. Reporting physisorption data for Gas/solid systems with special reference to the determination of surface area and porosity. Pure Appl Chem 1985;57:603–19.
[68] Pype J, Michielsen B, Seftel EM, Mullens S, Meynen V. Development of alumina microspheres with controlled size and shape by vibrational droplet coagulation. J Eur Ceram Soc 2017;37:189–98. https://doi.org/10.1016/j.jeurceramsoc.2016.07.020.
[69] Smrdel P, Bogataj M, Zega A, Planinšek O, Mrhar A. Shape optimization and characterization of polysaccharide beads prepared by ionotropic gelation. J Microencapsul 2008;25:90–105. https://doi.org/10.1080/02652040701776109.
[70] Gao H, Luo F, Deng H, Nan H, Qing Y. Fabrication of SiCf/SiC-mullite composite with improved pretreatment condition via precursor infiltration-sintering combined with infiltration-pyrolysis process. Ceram Int 2019;45:16062–9. https://doi.org/10.1016/j.ceramint.2019.05.122.
[71] Younis SA, Motawea EA, Moustafa YM, Lee J, Kim KH. A strategy for the efficient removal of chlorophenols in petrochemical wastewater by organophilic and aminated silica@alginate microbeads: taguchi optimization and isotherm modeling based on partition coefficient. J Hazard Mater 2020;397:122792. https://doi.org/10.1016/j.jhazmat.2020.122792.
[72] Hinić II, Stanišić GM, Popović ZV. Evolution of the surface and internal structure of Silica aerogels during the isothermal sintering process. In: Stojanović BD, Skorokhod VV, Nikolić MV, editors. Advanced science and technology of

sintering. Boston, MA: Springer US; 1999. p. 277–82. https://doi.org/10.1007/978-1-4419-8666-5. Advanced Science and Technology of Sintering.
[73] Chen YX, Li S, Mezari B, Hensen EJM, Yu R, Schollbach K, Brouwers HJH, Yu Q. Effect of highly dispersed colloidal olivine nano-silica on early age properties of ultra-high performance concrete. Cem Concr Compos 2022;131. https://doi.org/10.1016/j.cemconcomp.2022.104564.
[74] An J, Wang Y, Jia Q, Zhao F, Liu X. Microstructure and reactivity evolution of colloidal silica binder in different systems at elevated temperatures. Ceram Int 2020;46:20129–37. https://doi.org/10.1016/j.ceramint.2020.05.088.
[75] Salomão R, Fernandes L, Spera NCM. Combined effects of SiO2 ratio and purity on physical properties and microstructure of in situ alumina-mullite ceramic. Int J Appl Ceram Technol 2021;18:1702–9. https://doi.org/10.1111/ijac.13733.
[76] Yang HY, Yang YS, Choi HW. Non-isothermal crystallization kinetics of the BaTiO3-KNbO3-SiO2 glass. J Kor Phys Soc 2015;66:1125–9. https://doi.org/10.3938/jkps.66.1125.
[77] Wang P, Zhang Z, Yang G, Sun M, Li X, Wang Z. The structure and physical properties of peraluminous Li2O-Al2O3-SiO2 transparent glass-ceramics free of nucleating agents. J Non-Cryst Solids 2025;653. https://doi.org/10.1016/j.jnoncrysol.2025.123427.
[78] Chandrasekhar S, Pramada PN. Thermal studies of low silica zeolites and their magnesium exchanged forms. Ceram Int 2002;28:177–86. https://doi.org/10.1016/S0272-8842(01)00075-X.
[79] Chen YX, Li S, Mezari B, Hensen EJM, Yu R, Schollbach K, Brouwers HJH, Yu Q. Effect of highly dispersed colloidal olivine nano-silica on early age properties of ultra-high performance concrete. Cem Concr Compos 2022;131:104564. https://doi.org/10.1016/j.cemconcomp.2022.104564.
[80] Pagliari L, Dapiaggi M, Pavese A, Francescon F. A kinetic study of the quartz-cristobalite phase transition. J Eur Ceram Soc 2013;33:3403–10. https://doi.org/10.1016/j.jeurceramsoc.2013.06.014.
[81] Chaklader ACD. X-say Study of Quartz-Cristobalite transformation. J Am Ceram Soc 1963;46:66–71. https://doi.org/10.1111/j.1151-2916.1963.tb11677.x.
[82] Ma J, Xi X, He C, Chen W, Tian W, Li J, Wang C, Luo B, Shui A, Hua K. High-performance macro-porous alumina-mullite ceramic membrane supports fabricated by employing coarse alumina and colloidal silica. Ceram Int 2019;45:17946–54. https://doi.org/10.1016/j.ceramint.2019.06.012.
[83] Sternitzke M. Structural ceramic nanocomposites. J Eur Ceram Soc 1997;17:1061–82. https://doi.org/10.1016/S0955-2219(96)00222-1.
[84] Spera NCM, Fernandes L, Sakihama J, Santos Martinatti I, Tiba P, Salomão R. Designing colloidal silica-bonded porous structures of In-situ mullite for thermal insulation. Interceram: International Ceramic Review 2020;69:54–63. https://doi.org/10.1007/s42411-020-0120-x.
[85] Liang JJ, Lin QH, Zhang X, Jin T, Zhou YZ, Sun XF, Choi BG, Kim IS, Do JH, Jo CY. Effects of Alumina on cristobalite crystallization and properties of Silica-Based ceramic cores. J Mater Sci Technol 2017;33:204–9. https://doi.org/10.1016/j.jmst.2016.02.012.
[86] Bi Y, Zhang H, Wang H, Duan S, Jia Q, Ge S, Zhang S. Catalytic Fabrication of SiC/SiO2 coated graphite and its behaviour in Al2O3–C castable systems. Ceram Int 2019;45:16180–7. https://doi.org/10.1016/j.ceramint.2019.05.139.
[87] yong Wei H, Li H, Cui Y, li Sang R, yang Wang H, Wang P, long Bu J, xia Dong G. Synthesis of flexible mullite nanofibres by electrospinning based on nonhydrolytic sol–gel method. J Sol Gel Sci Technol 2017;82:718–27. https://doi.org/10.1007/s10971-017-4354-7.
[88] Gören R, Ersoy B, Özgür C, Alp T. Colloidal stability-slip casting behavior relationship in slurry of mullite synthesized by the USP method. Ceram Int 2012;38:679–85. https://doi.org/10.1016/j.ceramint.2011.07.056.
[89] Liu C, Shih K, Gao Y, Li F, Wei L. Dechlorinating transformation of propachlor through nucleophilic substitution by dithionite on the surface of alumina. J Soils Sediments 2012;12:724–33. https://doi.org/10.1007/s11368-012-0506-0.
[90] Song X, Ma Y, Wang J, Liu B, Yao S, Cai Q, Liu W. Homogeneous and flexible mullite nanofibers fabricated by electrospinning through diphasic mullite sol–gel route. J Mater Sci 2018;53:14871–83. https://doi.org/10.1007/s10853-018-2667-8.
[91] Liu D, Liu Z, Zou J, Li L, Sui X, Wang B, Yang N, Wang B. Synthesis and characterization of a hydroxyapatite-sodium alginate-chitosan scaffold for bone regeneration. Front Mater 2021;8. https://doi.org/10.3389/fmats.2021.648980.
[92] Kühne JH, Bartl R, Frisch B, Hammer C, Jansson V, Zimmer M. Bone formation in coralline hydroxyapatite: effects of pore size studied in rabbits. Acta Orthop 1994;65:246–52. https://doi.org/10.3109/17453679408995448.
[93] Anita Lett J, Sundareswari M, Ravichandran K. Porous hydroxyapatite scaffolds for orthopedic and dental applications - the role of binders. In: Mater today Proc. Elsevier Ltd; 2016. p. 1672–7. https://doi.org/10.1016/j.matpr.2016.04.058.
[94] Kimura R, Chatani S, Inui M, Motozuka S, Liu Z, Tagaya M. Control of biological surface States on chlorine-doped Amorphous Silica particles and their effective absorptive ability for antibody protein. Langmuir 2024;40:8939–49. https://doi.org/10.1021/acs.langmuir.4c00114.
[95] Kimura R, Chatani S, Inui M, Motozuka S, Yamada I, Tagaya M. Mechanochemical solid-state immobilization of photofunctional dyes on Amorphous Silica particles and investigation of their interactive mechanisms. Nanomaterials 2024;14. https://doi.org/10.3390/nano14090741.
[96] Kim HM, Himeno T, Kawashita M, Kokubo T, Nakamura T. The mechanism of biomineralization of bone-like apatite on synthetic hydroxyapatite: an in vitro assessment. J R Soc Interface 2004;1:17–22. https://doi.org/10.1098/rsif.2004.0003.
[97] Hornos F, Esquembre R, Gómez J. Competitive inhibition of protein adsorption to silica surfaces by their coating with high density charge polyelectrolytes. Colloids Surf B Biointerfaces 2020;191. https://doi.org/10.1016/j.colsurfb.2020.110993.
[98] Hasan A, Pattanayek SK, Pandey LM. Effect of functional groups of self-assembled monolayers on protein adsorption and initial cell adhesion. ACS Biomater Sci Eng 2018;4:3224–33. https://doi.org/10.1021/acsbiomaterials.8b00795.
[99] Narayan R, Colombo P, editors. Advances in bioceramics and porous ceramics VI. Daytona Beach: John Wiley & Sons; 2013.
[100] Vallet-Regí M. Bioceramics with clinical applications. John Wiley & Sons; 2014.
[101] Sousa LL, Souza ADV, Fernandes L, Arantes VL, Salomão R. Development of densification-resistant castable porous structures from in situ mullite. Ceram Int 2015;41:9443–54. https://doi.org/10.1016/j.ceramint.2015.03.328.
[102] Salomão R, Fernandes L. Porous co-continuous mullite structures obtained from sintered aluminum hydroxide and synthetic amorphous silica. J Eur Ceram Soc 2017;37:2849–56. https://doi.org/10.1016/j.jeurceramsoc.2017.03.017.
[103] Vijayan S, Wilson P, Prabhakaran K. Alumina foam microspheres by emulsion drop-casting in aqueous ammonium chloride solution. Ceram Int 2018;44:12547–54. https://doi.org/10.1016/j.ceramint.2018.04.051.
[104] Park J. Bioceramics: properties, characterizations, and applications. Iowa: Springer; 2008.
[105] Öhman C, Zwierzak I, Baleani M, Viceconti M. Human bone hardness seems to depend on tissue type but not on anatomical site in the long bones of an old subject. Proc Inst Mech Eng H 2013;227:200–6. https://doi.org/10.1177/0954411912459424.
[106] Li S, zhao Wang J, Yin B, sheng Hu Z, juan Zhang X, Wu W, bin Liu G, ke Liu Y, Fu L, ze Zhang Y. Atlas of suman Skeleton Hardness obtained using the micro-indentation technique. Orthop Surg 2021;13:1417–22. https://doi.org/10.1111/os.12841.
[107] Gao X, Feng X, Zhang D, Zhang J, Peng Y, Pan Z, Dai Z. Synthesis of high-performance mullite ceramics based on associated rare-earth kaolin. Int J Appl Ceram Technol 2023;20:1535–46. https://doi.org/10.1111/ijac.14311.
[108] Xu X, Li P, Wu J, Li Y, Zhang D, Qiu S. Preparation, microstructure and properties of solar thermal storage Nano-ZrO2-corundum-mullite composite ceramics. Ceram Int 2025. https://doi.org/10.1016/j.ceramint.2025.01.043.
[109] Singh S, Singh G, Bala N. Electrophoretic deposition of Fe3O4 nanoparticles incorporated hydroxyapatite-bioglass-chitosan nanocomposite coating on AZ91 Mg alloy. Mater Today Commun 2021;26:101870. https://doi.org/10.1016/J.MTCOMM.2020.101870.
[110] Santos KH, Ferreira JA, Osiro D, Conceição GJA, Filho RB, Colnago LA, de Jesus Agnolon Pallone EM. Influence of different chemical treatments on the surface of Al2O3/ZrO2 nanocomposites during biomimetic coating. Ceram Int 2017;43:4272–9. https://doi.org/10.1016/j.ceramint.2016.12.069.
[111] Vilardell AM, Cinca N, Garcia-Giralt N, Dosta S, Cano IG, Nogués X, Guilemany JM. In-vitro comparison of hydroxyapatite coatings obtained by cold spray and conventional thermal spray technologies. Mater Sci Eng C 2020;107. https://doi.org/10.1016/j.msec.2019.110306.
[112] Jiang T, Zhang Z, Zhou Y, Liu Y, Wang Z, Tong H, Shen X, Wang Y. Surface functionalization of titanium with chitosan/gelatin via electrophoretic deposition: characterization and cell behavior. Biomacromolecules 2010;11:1254–60. https://doi.org/10.1021/BM100050D.